Materials Chemistry and Physics 276 (2022) 125409

Contents lists available at ScienceDirect

Materials Chemistry and Physics

journal homepage: www.elsevier.com/locate/matchemphys

Design and development of (Ti, Zr, Hf)-Al based medium entropy alloys and high entropy alloys

Takeshi Nagase [a,b,c], Mitsuharu Todai [d], Pan Wang [e], Shi-Hai Sun [f,g], Takayoshi Nakano [b,g,*]

[a] Department of Materials and Synchrotron Radiation Engineering, Graduate School of Engineering, University of Hyogo, Himeji, Hyogo, 671-2280, Japan
[b] Division of Materials and Manufacturing Science, Graduate School of Engineering, Osaka University, Suita, Osaka, 565-0871, Japan
[c] Research Center for Ultra-High Voltage Electron Microscopy, Osaka University, Ibaraki, Osaka, 567-0047, Japan
[d] Department of Environmental Materials Engineering, National Institute of Technology, Niihama College, Ehime, 792-8580, Japan
[e] Singapore Institute of Manufacturing Technology, A*STAR, 637662, Singapore
[f] School of Materials Science and Engineering, Beijing Institute of Technology, Beijing, 100081, China
[g] Anisotropic Design & Additive Manufacturing Research Center, Osaka University, Suita, Osaka, 565-0871, Japan

HIGHLIGHTS

- The combination of 4th subgroup elements (Ti, Zr, Hf) and Al was investigated.
- $TiZrHfAlV_{0.2}$ and $TiZrHfAlNb_{0.2}$ HEAs were developed.
- Rapid solidification was effective to suppress the intermetallics formation.
- B2 ordering structure formation was detected by electron microscopy.

GRAPHICAL ABSTRACT

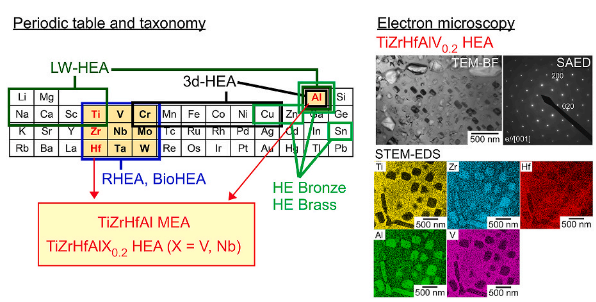

ARTICLE INFO

Keywords:
High entropy alloys
Alloy design
Rapid-solidification
Microstructure
Electron microscopy

ABSTRACT

The design and development of TiZrHfAl medium entropy alloy (MEA), and the $TiZrHfAlNb_{0.2}$ and $TiZrHfAlV_{0.2}$ high entropy alloys (HEAs) is described. The combination of 4th subgroup elements (Ti, Zr, and Hf) with Al is discussed based on the periodic table and taxonomy of HEAs. The alloys were designed using alloy parameters for HEAs, predicted ground state diagrams from the Materials Project, and the calculation of phase diagrams (CALPHAD). Rapid solidification was effective to suppress the formation of intermetallic compounds, resulting in BCC/B2 phase formation. Significant differences in the constituent phases and Vickers hardness between ingots and melt-spun ribbons were found among the TiZrHfAl MEA, $TiZrHfAlNb_{0.2}$, and $TiZrHfAlV_{0.2}$ HEAs.

1. Introduction

A new class of metallic materials, called high-entropy alloys (HEAs), has been developed in recent decades [1–7]. The taxonomy of HEAs and multicomponent alloys has been reported in detail in the literature [5]; HEAs can be grouped based on their main constituent elements and the relationship between the main constituent elements and their position in the periodic table. Fig. 1 shows the distribution of main constituent

* Corresponding author. Division of Materials and Manufacturing Science, Graduate School of Engineering, Osaka University, Suita, Osaka, 565-0871, Japan.
E-mail address: nakano@mat.eng.osaka-u.ac.jp (T. Nakano).

https://doi.org/10.1016/j.matchemphys.2021.125409
Received 21 June 2021; Received in revised form 31 August 2021; Accepted 3 November 2021
Available online 4 November 2021

elements in the periodic table for various HEAs including 3d-transition metal HEAs (3d-HEAs) [1,2,4,8,9], refractory HEAs (RHEAs) [10–14], HEAs for metallic biomaterials (BioHEAs) [15–21], light-weight HEAs (LW-HEAs) [22–26], and HE brasses and HE bronzes [27,28]. Al is the main-constituent element in 3d-HEAs as a body centered cubic (BCC) phase stabilizer in 3d-HEAs, LW-HEAs, and HE aluminium-bronzes. However, little attention has been paid to Al in RHEAs and BioHEAs, the main constituents of which are often similar and are found in subgroups 4–6. Some preliminary reports for HEAs including Ti, Zr, Hf and Al were as follows [29,30].: HCP-based HEA were obtained in Ti-Zr-Hf-Sc-Al HEA, and the addition of Al in Ti-Zr-Hf-Sc was effective to enhance the strength and ductility. Therefore, the combination of Al and 4th subgroup elements (Ti, Zr, and Hf) may offer a unique opportunity to develop new RHEA and/or BioHEA systems. In the present study, the successful fabrication of TiZrHfAl medium entropy alloy (MEA), $TiZrHfAlNb_{0.2}$ and $TiZrHfAlV_{0.2}$ HEAs by the alloy design based on the combination of Al and group 4 elements (Ti, Zr, Hf) and the application of rapid solidification was firstly reported.

2. Alloy design

The periodic table and the taxonomy of HEAs [5] indicates the particular characteristics of Al elements in HEAs (Fig. 1). As the first step of the alloy design focusing on the combination of Al element and main constituent elements of RHEAs and BioHEAs, the combination of 4th subgroup elements (Ti, Zr, Hf) and Al was considered, resulting in the design of a quaternary equiatomic TiZrHfAl alloy. Based on the entropy-based definition [6,7], the HEAs are defined as follows:

$$\Delta S_{mix} = -R\sum_{i=1}^{n} x_i \ln x_i \tag{1}$$

$$\Delta S_{mix} \geq 1.5R,\ HEAs \tag{2}$$

$$1.5\,R \geq \Delta S_{mix} \geq 1.0R,\ MEAs \tag{3}$$

$$1.0\,R \geq \Delta S_{mix},\ LEAs \tag{4}$$

where LEAs are low-entropy alloys, ΔS_{mix} is the mixing entropy of the ideal solution and regular solution, and x_i is the mole fraction of the i-th element. The ΔS_{mix} of an equiatomic TiZrHfAl alloy was 1.39R, where R is the gas constant. Based on the entropy-based alloy definition using ΔS_{mix}, an equiatomic TiZrHfAl alloy was classified as a medium-entropy alloy (MEA). To satisfy $\Delta S_{\text{mix}} \geq 1.5R$, the 5-component alloy systems of $TiZrHfAlV_x$ and $TiZrHfAlNb_x$ were considered, as Nb and V are widely used as constituent elements of RHEAs [14]. Nb was also used as one of the main constituent elements in BioHEAs [15–21], while V has not been used in BioHEAs as the main constituent element because of the Bio-incompatibility of V [31–34]. Fig. 2 shows the ΔS_{mix} as the function of x in $TiZrHfAlM_x$ alloys. The ΔS_{mix} increased with the increase in x value in $TiZrHfAlM_x$ alloys. To satisfy $\Delta S_{\text{mix}} \geq 1.5R$, $TiZrHfAlM_x$ alloys with $x =$ 0.2 ($TiZrHfAlNb_{0.2}$, $TiZrHfAlV_{0.2}$) were considered.

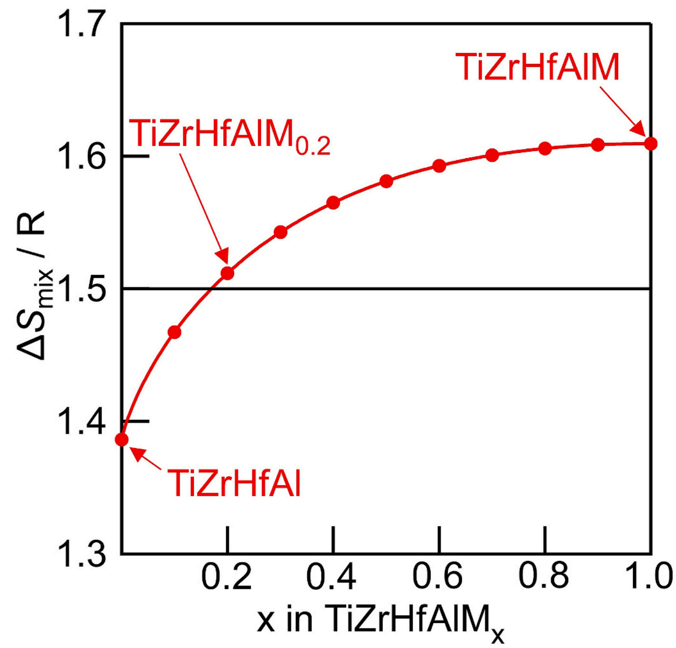

Fig. 2. The ΔS_{mix} as the function of x in $TiZrHfAlM_x$ alloys.

Various alloy parameters were suggested for the prediction of the S. S. formation tendency in multi-component alloys. The mixing enthalpy ΔH_{mix} [kJ/mol] [4,6,7], $\delta(\Delta H_{\text{mix}})$ [kJ/mol] [26], δ [4,6,7], and Ω [6,7,35,36] were calculated, where the detailed explanation of the alloy parameters was denoted in the other references [4,6,7,26,35,36]. The parameters of ΔH_{mix} and $\delta(\Delta H_{\text{mix}})$, which are related to the mixing enthalpy of the constituent elements, are given by,

$$\Delta H_{mix} = 4\sum_{i}\sum_{j,j\neq i} x_i \cdot x_j \cdot \Delta H_{i-j} \tag{5}$$

$$\delta(\Delta H_{mix}) = 4\sum_{i}\sum_{j,j\neq i} x_i \cdot x_j \cdot \left|\Delta H_{mix} - \Delta H_{i-j}\right| \tag{6}$$

where ($\Delta H_{i\text{-}j}$) is the mixing enthalpy of the i-j element pair, as shown in the literature [37]. ΔH_{mix} is the compositional average of $\Delta H_{i\text{-}j}$, whereas $\delta(\Delta H_{\text{mix}})$ corresponds to the degree of deviation of $\Delta H_{i\text{-}j}$. The dimensionless parameter, Ω, is given by,

$$\Omega = \frac{\overline{T_m} \cdot \Delta S_{mix}}{|\Delta H_{mix}|} \tag{7}$$

where $\overline{T_m}$ is the compositional average of the melting temperatures of the constituent elements. The dimensionless Ω parameter is used to

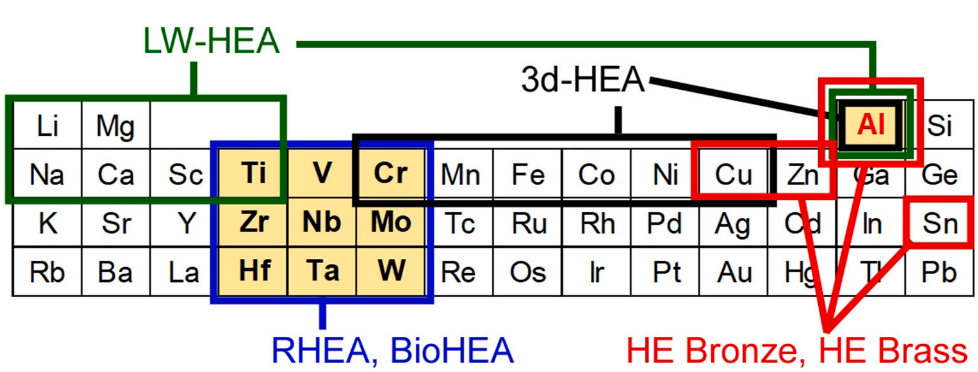

Fig. 1. Distribution of the main constituent elements in the periodic table for various high entropy alloys (HEAs) including 3d-HEAs, RHEAs, BioHEAs and LW-HEAs.

evaluate the ratio of enthalpy and entropy. The δ parameter is expressed as follows:

$$\delta = \sqrt{\sum_i x_i \cdot \left(1 - \frac{r_i}{\bar{r}}\right)^2} \quad (8)$$

where r_i was the atomic radius of i-th element and shown in the literature [37]. The $\bar{r}$ was the compositional average of r_i. The ΔH_{mix}, $\delta(\Delta H_{mix})$, and Ω parameters contain $\Delta H_{i\text{-}j}$, and δ includes r_i. The combination of $\Delta H_{i\text{-}j}$ and δ among the constituent elements is important for the design of the TiZrHfAl, TiZrHfAlV$_x$, and TiZrHfAlNb$_x$ alloys.

Fig. 3 shows the $\Delta H_{i\text{-}j}$ matrix and the value of atomic radius r for the Ti-Zr-Hf-Al-X (X = Nb, V) alloy system. In the $\Delta H_{i\text{-}j}$ matrix (Fig. 3a) for 4th subgroup elements and Al, the $\Delta H_{i\text{-}j}$ for i = Al, j = Ti, Zr, or Hf show the largest negative values. Large negative values were also observed in $\Delta H_{i\text{-}j}$ for i = Al, j = V and Nb. A large negative $\Delta H_{i\text{-}j}$ corresponds to the existence of various intermetallic compounds in the binary phase diagrams of Al-Ti [38,39], Al-Zr [40,41], Al-Hf [42,43], Al-V [44], and Al-Nb [45]. In contrast, $\Delta H_{i\text{-}j}$ among all combinations without Al is comparatively low. In the other words, the absolute value of $\Delta H_{i\text{-}j}$ among Ti, Zr, and Hf, and of $\Delta H_{i\text{-}j}$ when i = Ti, Zr, Hf and j = V, Nb was comparatively low. In the values of r (Fig. 3b), the difference of r among Zr and Hf, and that among Ti, Al and Nb, was relatively small.

Table 1 shows the empirical alloy parameters of $\Delta S_{mix}/R$ [6,7], ΔH_{mix} [kJ/mol] [4,6,7], $\delta(\Delta H_{mix})$ [kJ/mol] [26], δ [4,6,7], and Ω [6,7,35,36] in TiZrHfAl, TiZrHfAlV$_{0.2}$, and TiZrHfAlNb$_{0.2}$ alloys together with equiatomic TiZrHf, CoCrFeMnNi [1] as a typical example of 3d-HEAs, TiNbTaZrHf [12,13] as a typical example of RHEAs, and TiNbTaZrMo [15,16] as a typical example of BioHEAs. TiZrHfAl, TiZrHfAlV$_{0.2}$, and TiZrHfAlNb$_{0.2}$ alloys show the large negative values below −20 kJ/mol for ΔH_{mix}, and the large positive values for $\delta(\Delta H_{mix})$. These characteristics of ΔH_{mix} and $\delta(\Delta H_{mix})$ for TiZrHfAl, TiZrHfAlV$_{0.2}$, and TiZrHfAlNb$_{0.2}$ alloys differ from the typical HEAs of CoCrFeMnNi, TiNbTaZrHf, and TiZrNbTaMo which have significantly smaller absolute values of ΔH_{mix} and $\delta(\Delta H_{mix})$. The ΔH_{mix} and $\delta(\Delta H_{mix})$ in equiatomic TiZrHf was nearly zero. The value of Ω in TiZrHfAl, TiZrHfAlV$_{0.2}$, and TiZrHfAlNb$_{0.2}$ alloys was below 1.1, which is the threshold value for HEAs [35,36]. The δ parameter relates to the difference in r_i between the constituent elements. In TiZrHfAl, TiZrHfAlV$_{0.2}$, and TiZrHfAlNb$_{0.2}$, δ was below 6.5, which is below the threshold value for a high tendency to form S.S. in HEAs [4,6,7]. The above results imply that the combination of Al and 4th subgroup elements (Ti, Zr, Hf) is not suitable for S.S. formation according to their empirical alloy parameters of ΔH_{mix}, $\delta(\Delta H_{mix})$, and Ω.

Table 1
Empirical alloy parameters of ΔS_{mix}/R, ΔH_{mix}, $\delta(\Delta H_{mix})$, δ, and Ω in TiZrHfAl, TiZrHfAlV$_{0.2}$ and TiZrHfAlNb$_{0.2}$ alloys, together with equiatomic TiZrHf, CoCrFeMnNi as a typical example of 3d-HEAs, TiNbTaZrHf as a typical example of RHEAs, and TiNbTaZrMo as a typical example of BioHEAs.

Alloys	ΔS_{mix}/R	ΔH_{mix} [kJ/mol]	$\delta(\Delta H_{mix})$ [kJ/mol]	δ [%]	Ω
CoCrFeMnNi	1.61	−4.2	4.9	4.2	5.8
TiNbTaZrHf	1.61	2.7	2.6	5.5	12.4
TiNbTaZrMo	1.61	−1.8	5.9	5.9	19.7
TiZrHf	1.10	0.0	0.0	4.3	–
TiZrHfAl	1.39	−28.3	28.3	5.3	0.8
TiZrHfAlV0.2	1.51	−26.7	29.4	6.0	0.9
TiZrHfAlNb0.2	1.51	−26.0	30.0	5.4	0.9

The S.S. forming tendency in the TiZrHfAl, TiZrHfAlNb$_{0.2}$, and TiZrHfAlV$_{0.2}$ alloys are further discussed based on the alloy parameters as a function of ΔS_{mix}. Fig. 4 shows the alloy parameters of ΔH_{mix}, $\delta(\Delta H_{mix})$, and δ as a function of ΔS_{mix} in the quaternary Ti-Zr-Hf-Al alloys. Approximately 1.3 $\times$ 10^7 combinations of compositions were calculated and the green dots denote the alloys satisfying the condition, $\Delta S_{mix} \geq 1.0R$. The equiatomic composition alloys of ternary TiZrHf and quaternary TiZrHfAl are indicated by the red-open circles. The regions denoted by the red rectangular heads with the indexes M1 ($\Delta S_{mix} \geq 1.0R$ and $5 \geq \Delta H_{mix} \geq -5$), M2 ($\Delta S_{mix} \geq 1.0R$ and $10 \geq \delta(\Delta H_{mix})$), and M3 ($\Delta S_{mix} \geq 1.0R$ and $6.5 \geq \delta$) indicate the MEAs with a high S.S. formation tendency. The equiatomic TiZrHf alloy is positioned in the regions M1 (Fig. 4a), M2 (Fig. 4b), and M3 (Fig. 4c), indicating its high S.S. formation tendency. Single S.S. formation in arc-melted ingots of ternary TiZrHf has been reported in the literature [18]. The equiatomic TiZrHfAl alloy is positioned out of the M1 (Fig. 4a) and M2 (Fig. 4b) regions, indicating a low S.S. formation tendency due to the alloy parameters related to $\Delta H_{i\text{-}j}$. In contrast, the equiatomic TiZrHfAl alloy is positioned in region M3 (Fig. 4c), indicating a high S.S. formation tendency from the view point of the difference in r_i among the constituent elements. Focusing on the green dots in alloys including equiatomic and non-equiatomic alloys, a number of alloys are positioned out of the M1 (Fig. 4a) and M2 (Fig. 4b) regions, regardless the value of ΔS_{mix}. In contrast, all green dots are positioned in the M3 region (Fig. 4c) regardless the value of ΔS_{mix}. The quaternary Ti-Zr-Hf-Al alloy system shows a high S.S. formation tendency from the viewpoint of the δ

(a) $\Delta H_{i\text{-}j}$ [kJ/mol]

	Ti	Zr	Hf	Al	V	Nb
Ti		0	0	-30	-2	2
Zr			0	-44	-4	4
Hf				-39	-2	4
Al					-16	-18
V						-1
Nb						

(b) r [nm]

Ti	0.147
Zr	0.162
Hf	0.16
Al	0.143
V	0.132
Nb	0.143

Fig. 3. Matrix of the mixing enthalpy of i-j atomic pair ($\Delta H_{i\text{-}j}$) and atomic radius (r_i) for the Ti-Zr-Hf-Al-X (X = Nb, V) alloy system. (a) $\Delta H_{i\text{-}j}$, (b) r_i.

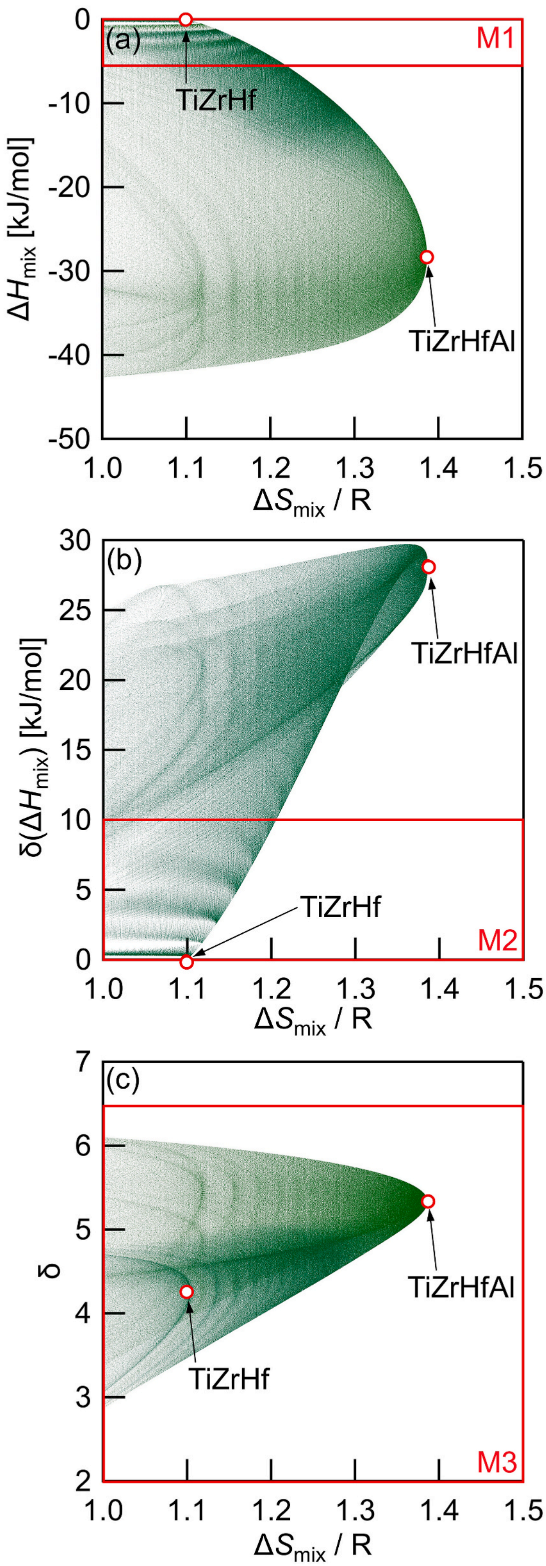

Fig. 4. Empirical alloy parameters, ΔH_{mix}, $\delta(\Delta H_{mix})$, and δ, as a function of ΔS_{mix} in Ti-Zr-Hf-Al alloys. Green dots indicate Ti-Zr-Hf-Al alloys of approximately 1.3 $\times$ 10^7 different composition combinations. Red-open circles correspond to the equiatomic TiZrHf and TiZrHfAl alloys. (a) ΔH_{mix}, (b) $\delta(\Delta H_{mix})$, (c) δ. The red rectangles denote regions associated with indexes M1 ($\Delta S_{mix} \geq 1.0R$ and $5 \geq \Delta H_{mix} \geq -5$), M2 ($\Delta S_{mix} \geq 1.0R$ and $10 \geq \delta(\Delta H_{mix})$), and M3 ($\Delta S_{mix} \geq 1.0R$ and $6.5 \geq \delta$). (For interpretation of the references to colour in this figure legend, the reader is referred to the Web version of this article.)

parameter (Fig. 4c), while an opposite tendency from the viewpoint of ΔH_{mix} and $\delta(\Delta H_{mix})$ (Fig. 4a and b). The large negative values in $\Delta H_{i\text{-}j}$ for i = Al, j = Ti, Zr, or Hf (Fig. 3) are the origin of the large negative ΔH_{mix} and large positive $\delta(\Delta H_{mix})$ in the quaternary Ti-Zr-Hf-Al alloy system.

Fig. 5 shows the alloy parameters of ΔH_{mix}, $\delta(\Delta H_{mix})$, and δ as a function of ΔS_{mix} in the 5-component Ti-Zr-Hf-Al-Nb (Fig. 5a) and Ti-Zr-Hf-Al-V (Fig. 5b) alloys. Approximately 1.3 $\times$ 10^7 combinations of compositions were calculated and shown as green dots. The regions within the red rectangle and the indexes H1 ($\Delta S_{mix} \geq 1.5R$ and $5 \geq \Delta H_{mix} \geq$ -5), H2 ($\Delta S_{mix} \geq 1.5R$ and $10 \geq \delta(\Delta H_{mix})$), and H3 ($\Delta S_{mix} \geq 1.5R$ and $6.5 \geq \delta$) indicate HEAs with high S.S. formation tendency. Of the Ti-Zr-Hf-Al-Nb alloys, only few can exist in the regions H1 (Fig. 5a1) and H2 (Fig. 5a2). In contrast, all green dots corresponding to Ti-Zr-Hf-Al-Nb alloys existed in the region H3 (Fig. 5a3). Focusing on the equiatomic TiZrHfAlNb and non-equiatomic $TiZrHfAlNb_{0.2}$ alloys, both of them tend to have a larger negative ΔH_{mix} value (Fig. 5a1) and larger positive $\delta(\Delta H_{mix})$ value (Fig. 5a2) among all the alloys. These indicate that the Ti-Zr-Hf-Al-Nb alloy system exhibits a low S.S. formation tendency because of the large negative ΔH_{mix} and large positive $\delta(\Delta H_{mix})$, and the S.S. formation tendency of non-equiatomic $TiZrHfAlNb_{0.2}$ alloy is lower among the Ti-Zr-Hf-Al-Nb alloys with $\Delta S_{mix} \geq 1.5R$. The significant differences in the distribution of green dots was not observed between Fig. 5a1 (Ti-Zr-Hf-Al-Nb) and Fig. 5b1 (Ti-Zr-Hf-Al-V) focusing on ΔH_{mix}, and that between Fig. 5a2 (Ti-Zr-Hf-Al-Nb) and Fig. 5b2 (Ti-Zr-Hf-Al-V) focusing on $\delta(\Delta H_{mix})$. In contrast, the distribution of green dots in Fig. 5b3 (Ti-Zr-Hf-Al-V), focusing on δ, is different from that in Fig. 5a3 (Ti-Zr-Hf-Al-Nb). Most of green dots in Ti-Zr-Hf-Al-V alloys with $\Delta S_{mix} \geq 1.5R$ are positioned out of the H3 region in Fig. 5b3. It should be noted here that the value of δ parameter of the non-equiatomic $TiZrHfAlV_{0.2}$ is on the low side among the Ti-Zr-Hf-Al-V alloys with $\Delta S_{mix} \geq 1.5R$ and in the H3 region. Fig. 5 clarifies that both the Ti-Zr-Hf-Al-Nb (Fig. 5a) and Ti-Zr-Hf-Al-V (Fig. 5b) alloys exhibit a low S.S. formation tendency regardless the alloy composition because of the large negative ΔH_{mix} and large positive $\delta(\Delta H_{mix})$ parameters. Focusing on the δ parameter, most of the Ti-Zr-Hf-Al-V alloys are positioned out of the H3 region, while non-equiatomic $TiZrHfAlV_{0.2}$ alloys are positioned in the H3 region in Fig. 5b3. Thus, alloys that simultaneously satisfy the high S.S. formation tendency criterion according to the alloy parameters of ΔH_{mix}, $\delta(\Delta H_{mix})$, and δ cannot be designed for the Ti-Zr-Hf-Al-Nb (Fig. 5a) and Ti-Zr-Hf-Al-V (Fig. 5b) alloys.

The predicted ground states at 0 K in the calculated ground state diagrams based on the database of *ab-initio* calculations obtained from the Materials Project [46] were determined to be useful in the alloy design of the various multi-component amorphous alloys [47] and HEAs [48–51]. Fig. 6 shows the predicted ground states in the quaternary phase diagrams at 0 K constructed using the Materials Project. In Fig. 6a, a number of compounds are seen in the quaternary Ti-Zr-Hf-Al phase diagram, corresponding to the existence of intermetallic compounds in the binary phase diagrams of Al-Ti [39,40], Al-Zr [41,42], and Al-Hf [43,44]. Ternary and quaternary intermetallics were not detected in the quaternary Ti-Zr-Hf-Al (Fig. 6a) and ternary Ti_3Al-Zr_3Al-Hf_3Al (Fig. 6b) phase diagrams. Ternary and quaternary intermetallics were also not observed in Ti_3Al-Zr_3Al-Hf_3Al-Nb (Fig. 6c) and Ti_3Al-Zr_3Al-Hf_3Al-V (Fig. 6d) phase diagrams. This implies that the possibility of formation of multi-component ternary and/or quaternary intermetallic compounds was not as high in TiZrHfAl, $TiZrHfAlV_{0.2}$, and $TiZrHfAlNb_{0.2}$ alloys.

Thermodynamic calculations using FactSage version 7.3 [52] and the SGTE2017 [53] database were performed to predict the tendency to form S.S. in TiZrHfAl, $TiZrHfAlV_{0.2}$, and $TiZrHfAlNb_{0.2}$ alloys. In the SGTE2017 database [53], the binary atomic pairs of Hf-Al and Hf-V were not assessed in the Ti-Zr-Hf-Al, Ti-Zr-Hf-Al-V, and Ti-Zr-Hf-Al-Nb alloy systems. Fig. 7 shows the thermodynamic calculation results in the Ti-Zr-Al, Ti-Zr-Al-Nb, and Ti-Zr-Al-V alloy systems as alternatives to Ti-Zr-Hf-Al, Ti-Zr-Hf-Al-Nb, and Ti-Zr-Hf-Al-V, where Hf was replaced by Ti and Zr. Fig. 8 shows the thermodynamic calculation results for

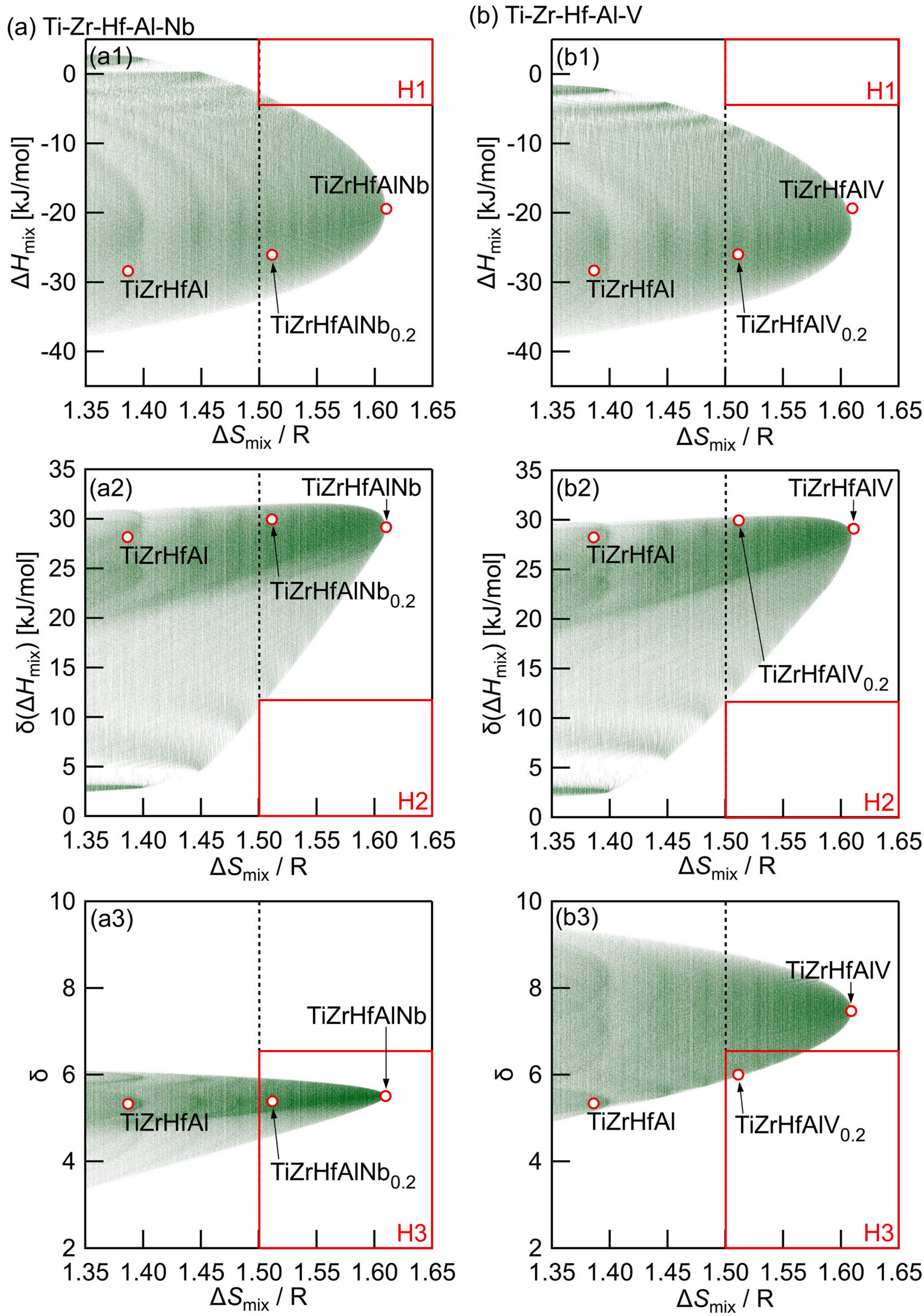

Fig. 5. Empirical alloy parameters, ΔH_{mix}, $\delta(\Delta H_{mix})$, and δ, as a function of ΔS_{mix} in Ti-Zr-Hf-Al-Nb (a) and Ti-Zr-Hf-Al-V (b) alloys. Green dots indicate approximately 1.3×10^7 specific alloy compositions for the Ti-Zr-Hf-Al-Nb (a) and Ti-Zr-Hf-Al-V (b) alloys. Red-open circles correspond to the equiatomic TiZrHfAl, TiZrHfAlNb, TiZrHfAlV, and non-equiatomic $TiZrHfAlNb_{0.2}$ and $TiZrHfAlV_{0.2}$ alloys. (a1) (b1) ΔH_{mix}, (a2) (b2) $\delta(\Delta H_{mix})$, (a3) (b3) δ. Red rectangles denote regions associated with indexes H1 ($\Delta S_{mix} \geq 1.5R$ and $5 \geq \Delta H_{mix} \geq -5$), H2 ($\Delta S_{mix} \geq 1.5R$ and $10 \geq \delta(\Delta H_{mix})$), and H3 ($\Delta S_{mix} \geq 1.5R$ and $6.5 \geq \delta$). (For interpretation of the references to colour in this figure legend, the reader is referred to the Web version of this article.)

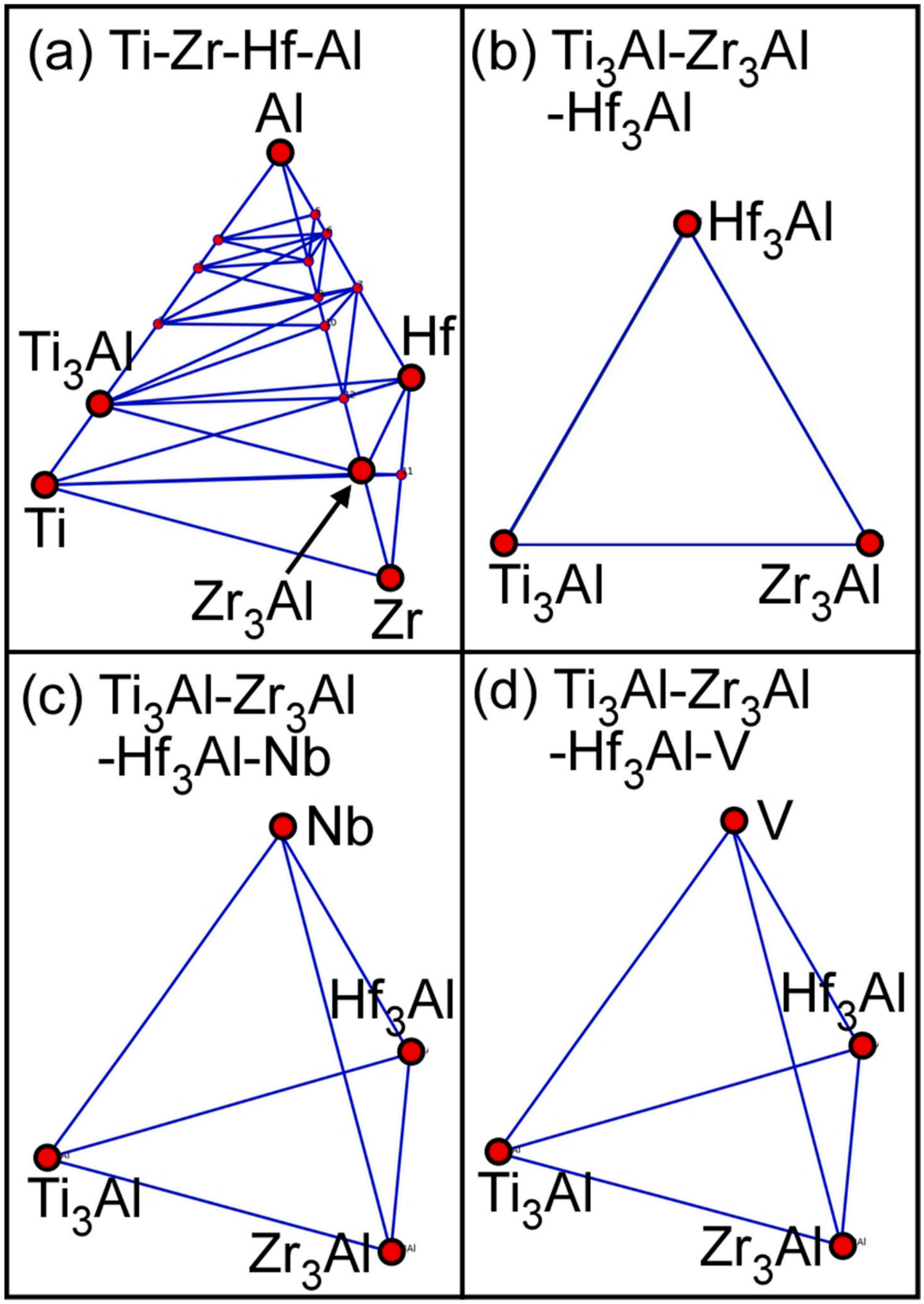

Fig. 6. Predicted ground states in quaternary phase diagrams at 0 K using Materials Project for (a) Ti-Zr-Hf-Al, (b) Ti_3Al-Zr_3Al-Hf_3Al, (c) Ti_3Al-Zr_3Al-Hf_3Al-Nb, and (d) Ti_3Al-Zr_3Al-Hf_3Al-V.

TiZrHfAl, $TiZrHfAlV_{0.2}$, and $TiZrHfAlNb_{0.2}$ alloys for reference only. Fig. 7 shows the calculated phase diagrams in $Ti_{3-x}Zr_xAl$, $Ti_{3-x}Zr_xAlNb_{0.2}$, and $Ti_{3-x}Zr_xAlV_{0.2}$ as alternatives to TiZrHfAl, $TiZrHfAlNb_{0.2}$, and $TiZrHfAlV_{0.2}$. In Fig. 7a, the BCC phase exists at temperatures below the solidus temperature (T_S) regardless of the Ti/Zr ratio in the $Ti_{3-x}Zr_xHfAl$ alloy. The BCC phase was not stable in the low temperature region and transforms into the HCP phase as the temperature decreasing in the $Ti_{3-x}Zr_xHfAl$ alloy. A BCC single phase region was also observed at temperatures below T_S in $Ti_{3-x}Zr_xAlNb_{0.2}$ (Fig. 7b) and $Ti_{3-x}Zr_xAlV_{0.2}$ (Fig. 7c). A two-phase BCC and HCP region exists at low temperatures for $Ti_{3-x}Zr_xAlNb_{0.2}$ (Fig. 7b) and $Ti_{3-x}Zr_xAlV_{0.2}$ (Fig. 7c). The temperature range of the single BCC phase in $Ti_{3-x}Zr_xAlNb_{0.2}$ (Fig. 7b) and $Ti_{3-x}Zr_xAlV_{0.2}$ (Fig. 7c) was larger than in $Ti_{3-x}Zr_xAl$ (Fig. 7a). The addition of Nb and V in $Ti_{3-x}Zr_xAl$ effectively stabilized the BCC phase, which corresponds to the BCC stabilization in Ti alloys by V and Nb addition [54,55]. Fig. 8 shows the equilibrium calculation results in TiZrHfAl, $TiZrHfAlNb_{0.2}$, and $TiZrHfAlV_{0.2}$. The existence of the BCC phase at temperatures below T_S and the decomposition of the BCC phase to the HCP phase with decreasing temperature was observed. Thermodynamic calculation results imply the possibility of S.S. formation in TiZrHfAl, $TiZrHfAlNb_{0.2}$, and $TiZrHfAlV_{0.2}$. Based on these results, the solidification microstructure in arc-melted ingots and rapidly-solidified specimens of melt-spun ribbons of TiZrHfAl, $TiZrHfAlNb_{0.2}$, and $TiZrHfAlV_{0.2}$ was investigated focusing on BCC phase formation.

3. Experimental procedures

Three alloys, TiZrHfAl ($Ti_{25}Zr_{25}Hf_{25}Al_{25}$, at.%), $TiZrHfAlNb_{0.2}$ ($Ti_{23.8}Zr_{23.8}Hf_{23.8}Al_{23.8}Nb_{4.76}$, at.%), and $TiZrHfAlV_{0.2}$ ($Ti_{23.8}Zr_{23.8}Hf_{23.8}Al_{23.8}V_{4.76}$, at.%), were designed. Arc-melted ingots were prepared

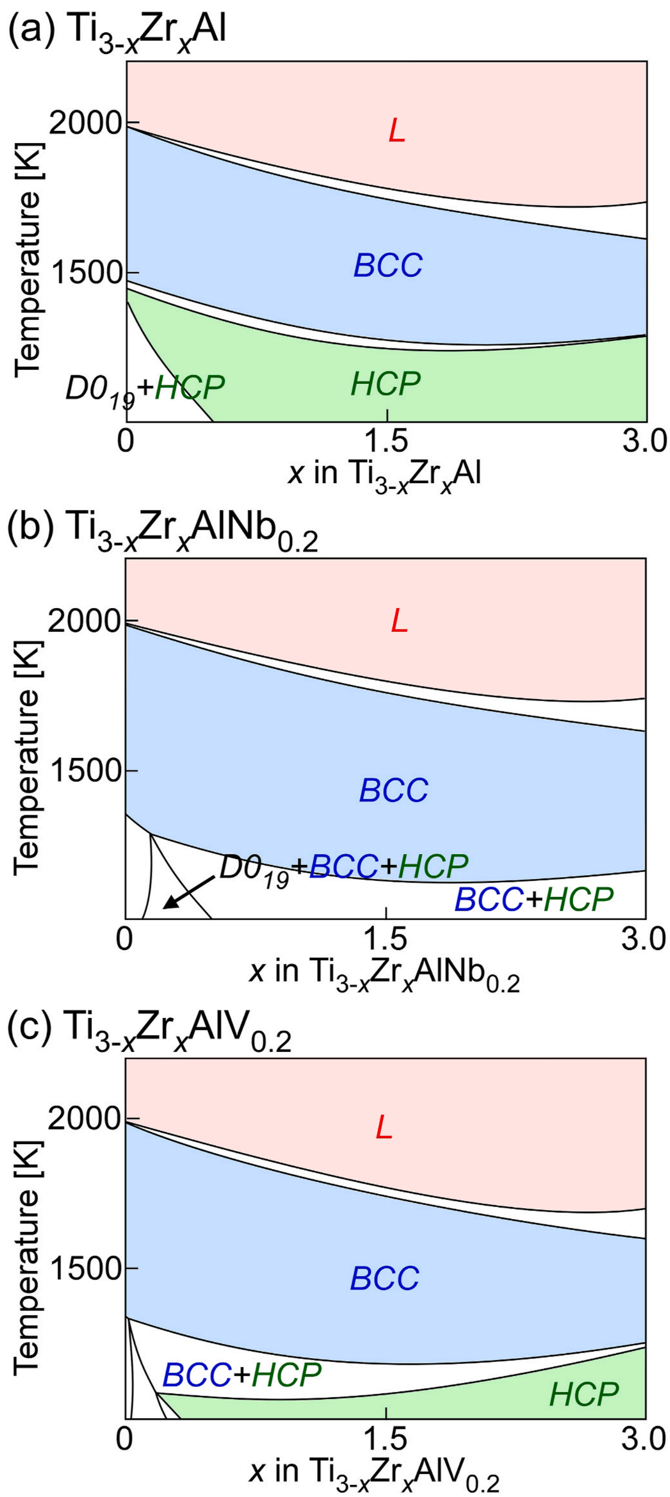

Fig. 7. Calculated phase diagrams for (a) $Ti_{3\text{-}x}Zr_xHfAl$, (b) $Ti_{3\text{-}x}Zr_xAlNb_{0.2}$, and (c) $Ti_{3\text{-}x}Zr_xHfAlV_{0.2}$ as alternatives to TiZrHfAl, $TiZrHfAlNb_{0.2}$, and $TiZrHfAlV_{0.2}$ using FactSage ver 7.3 and SGTE2017.

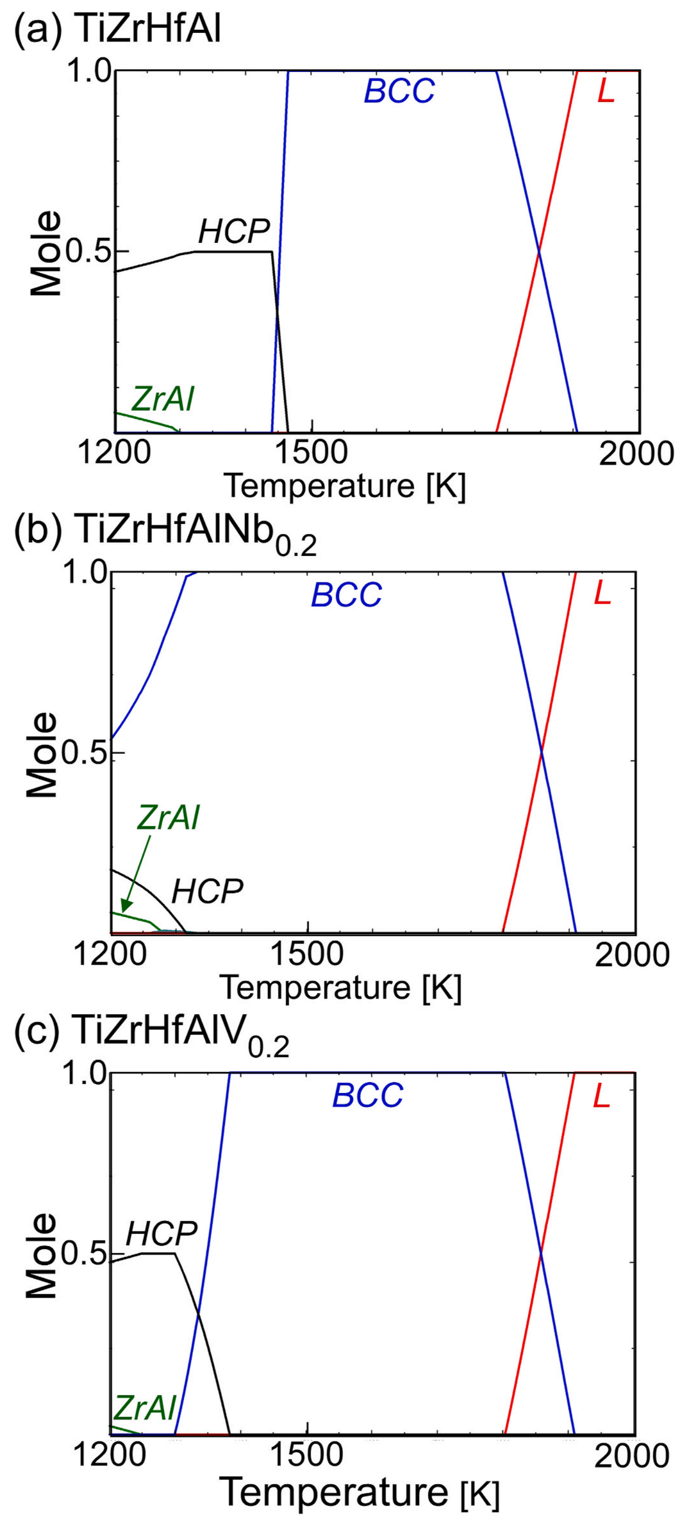

Fig. 8. Equilibrium calculation results in (a) TiZrHfAl, (b) $TiZrHfAlNb_{0.2}$, and (c) $TiZrHfAlV_{0.2}$ using FactSage ver 7.3 and the SGTE2017 database. In the SGTE2017 database, assessment of the binary pairs of Hf-Al and Hf-V were not performed. The results should be used as reference.

by mixing pure element lumps. The purity of the Ti, Zr, Nb, and V was above 99.9% (3 N), while that of the Hf was above 2 N. The experimentally-estimated cooling rate (*CR*) during solidification in the arc-melting process was approximately 2000 K/s [56]. The *CR* during the arc-melting using water-cooled Cu hearth was estimated to be an order of magnitude higher than that in the metallic mold casting (centrifugal metallic mold casting) [57]. Rapidly-solidified specimens of melt-spun ribbons were also prepared by a single-roller melt-spinning method from part of the arc-melted ingots, where the *CR* during the single-roller melt-spinning method was reported to be on the order of 10^5 K/s in literature [58,59]. The constituent phases of the ingots and melt-spun ribbons were investigated by x-ray diffraction (XRD) analysis and transmission electron microscopy (TEM). The solidification microstructures of the ingots and melt-spun ribbons were investigated by scanning electron microscopy (SEM), electron probe microanalysis - wave dispersive spectroscopy (EPMA-WDS), TEM, and scanning transmission electron microscopy (STEM). TEM and STEM specimens were prepared by ion-milling using Ar ions at room temperature. A micro-Vickers hardness (H_V) test with a test force of 500gf and 1 kgf was performed to evaluate the hardness of arc-melted ingots and melt-spun ribbons.

4. Results and discussion

Fig. 9 shows the XRD patterns of the arc-melted ingots in TiZrHfAl, $TiZrHfAlNb_{0.2}$, and $TiZrHfAlV_{0.2}$. The calculated X-ray intensity of Ti_3Al, Zr_3Al, Hf_3Al, and Zr_2Al [60–63] was also shown in Fig. 9. The calculated XRD intensity was obtained using VESTA [64]. Sharp peaks in the arc-melted ingots of TiZrHfAl, $TiZrHfAlNb_{0.2}$, and $TiZrHfAlV_{0.2}$ cannot be indexed as the BCC phase, Ti_3Al, Zr_3Al and Hf_3Al. The inset shows the element mapping using EPMA-WDS of the arc-melted ingots in $TiZrHfAlV_{0.2}$ as a typical example of the elemental distribution in the ingots. The macroscopic elemental distribution was not detected. In the XRD patterns (Fig. 9), most of peaks appear to correspond to Zr_2Al [60–63], and the formation of $Zr_2(Al, Sc)$ in the ingots was also reported in $Ti_{25}Zr_{25}Hf_{25}Sc_{15}Al_{10}$ HEA [30]. In the present study, further investigation of the XRD patterns was not performed in the arc-melted ingots because they did not contain S.S. formation.

Fig. 10 shows the XRD patterns of the melt-spun ribbons in TiZrHfAl, $TiZrHfAlNb_{0.2}$, and $TiZrHfAlV_{0.2}$. The calculated X-ray intensity of various binary Zr-Al intermetallic compounds including Zr_3Al, Zr_2Al [60–62], Zr_2Al_3, Zr_4Al_3, Zr_5Al_3, $ZrAl_2$, and $ZrAl_3$ was also shown in Fig. 10. Most of the high intensity peaks can be identified as the BCC

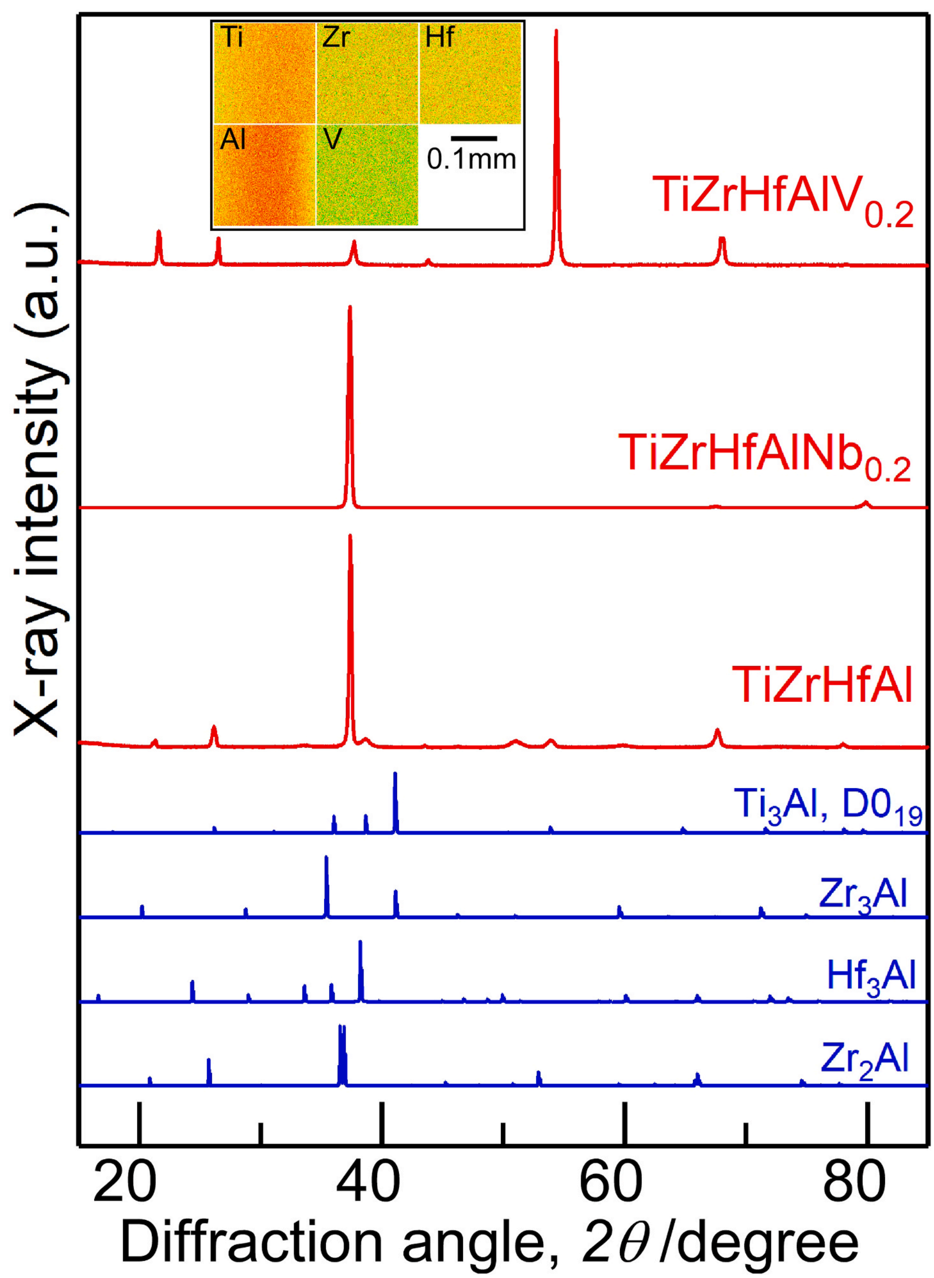

Fig. 9. XRD patterns of the arc-melted ingots in TiZrHfAl, $TiZrHfAlNb_{0.2}$, and $TiZrHfAlV_{0.2}$ together with the calculated x-ray intensity of Ti_3Al, Zr_3Al, Hf_3Al, and Zr_2Al. The inset shows the elemental mapping using electron probe microanalysis – wavelength dispersive spectroscopy (EPMA-WDS) of the arc-melted ingots in $TiZrHfAlV_{0.2}$.

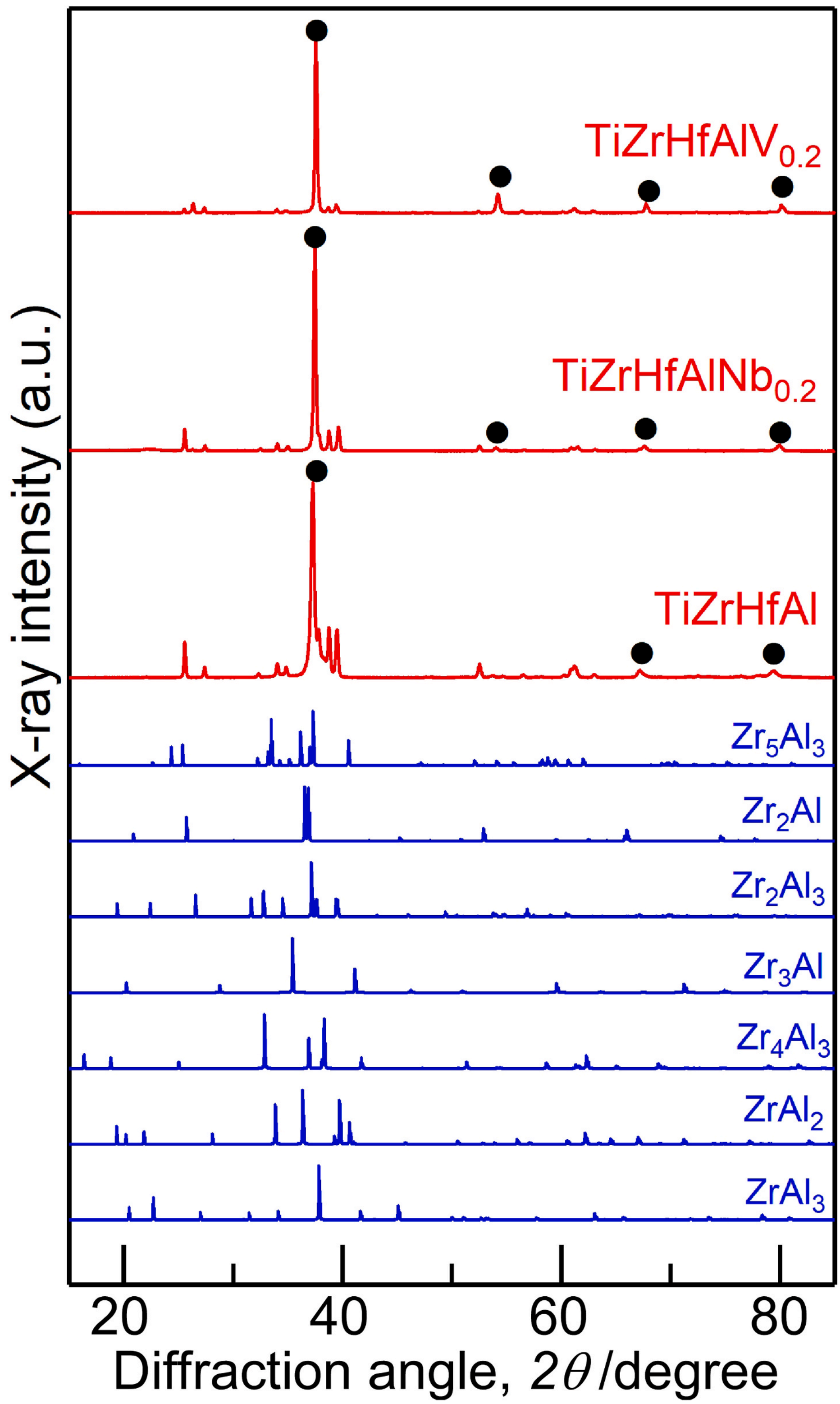

Fig. 10. XRD patterns of the rapidly-solidified melt-spun ribbons in TiZrHfAl, $TiZrHfAlNb_{0.2}$, and $TiZrHfAlV_{0.2}$ together with the calculated x-ray intensity of various Zr-Al intermetallic compounds.

phase, as indicated by the black closed circle (●). Minor peaks, which cannot be indexed as BCC phase, were also observed in TiZrHfAl, $TiZrHfAlNb_{0.2}$, and $TiZrHfAlV_{0.2}$. The number and intensity of the minor peaks in $TiZrHfAlV_{0.2}$ were smallest among TiZrHfAl, $TiZrHfAlNb_{0.2}$, and $TiZrHfAlV_{0.2}$. To investigate the more-detailed solidification microstructure in the melt-spun ribbons, TEM and STEM observations was performed with particular attention on $TiZrHfAlV_{0.2}$.

Fig. 11 shows TEM bright field (BF) images and selected area diffraction (SAED) patterns of the melt-spun ribbons of TiZrHfAl, $TiZrHfAlNb_{0.2}$, and $TiZrHfAlV_{0.2}$. Not a single phase microstructure, but a composite structure composed of a crystalline matrix with crystalline precipitates was observed in the TEM-BF images of TiZrHfAl (Fig. 11a),

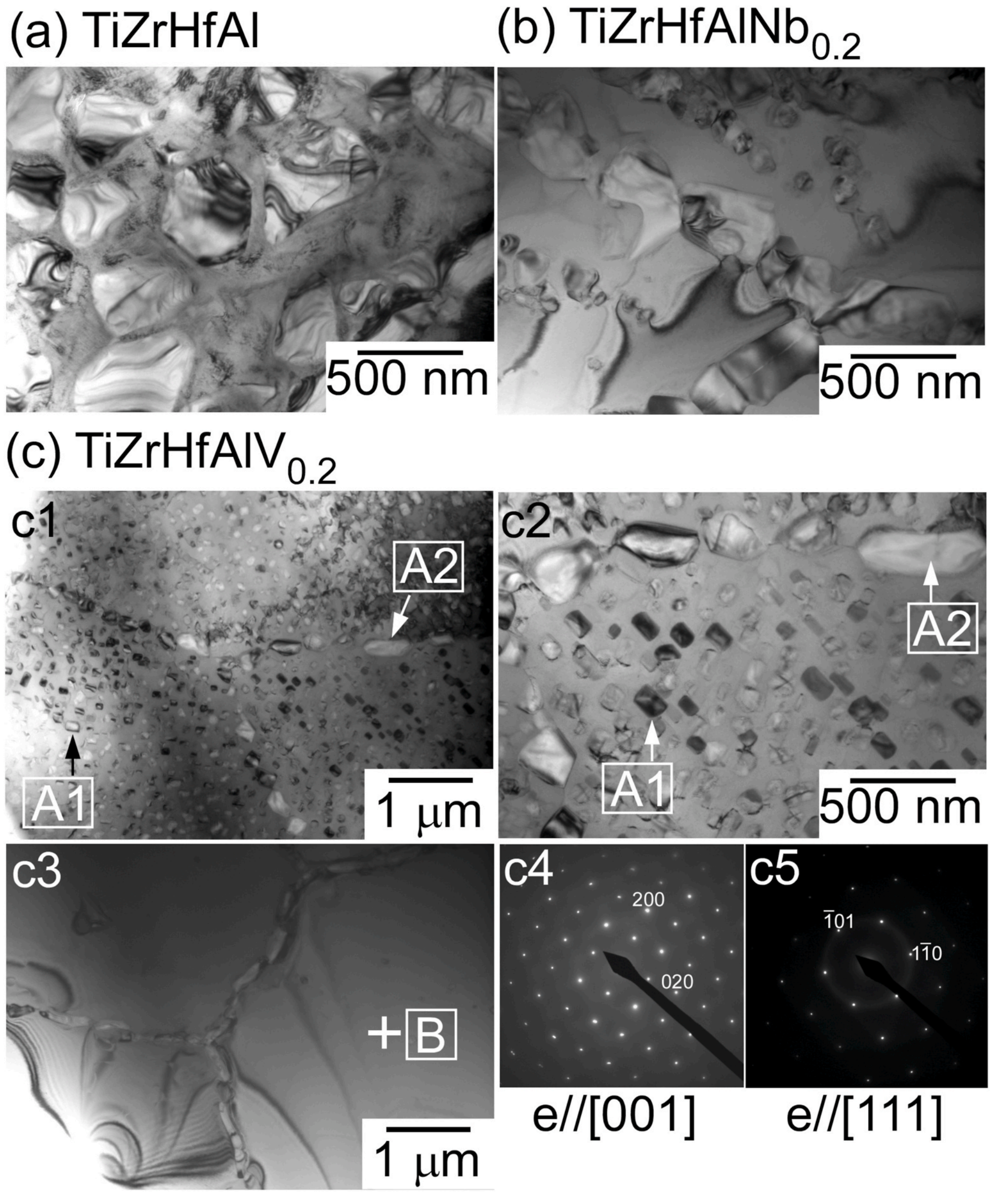

Fig. 11. Transmission electron microscopy bright field (TEM-BF) images and selected area electron diffraction (SAED) patterns of the rapidly-solidified melt-spun ribbons in (a) TiZrHfAl, (b) $TiZrHfAlNb_{0.2}$, and (c) $TiZrHfAlV_{0.2}$. Further investigation of $TiZrHfAlV_{0.2}$ are shown as a (c1) BF image, (c2) magnified image of Fig. 11c3, (c3) BF image, and (c4) (c5) SAED patterns obtained from the position (index A) in Fig. 11c3.

$TiZrHfAlNb_{0.2}$ (Fig. 11b), $TiZrHfAlV_{0.2}$ (Figs. 11c1, c2, and c3). Focusing on $TiZrHfAlV_{0.2}$, two types of TEM-BF images were observed in the melt-spun ribbons. (1) The composite structure of the matrix and precipitates, where the precipitates embedded in the grain are indicated by the index A1 and those at grain boundaries are indicated by the index A2, were observed as shown in Figs. 11c1 and c2. (2) The composite structure of the matrix and precipitates, where precipitates were observed only at the grain boundary, as shown in Fig. 11c3. Figs. 11c4 and c5 shows the SAED patterns obtained from position B in Fig. 11c3 without precipitates. The diffraction spots can be indexed as BCC-based B2-ordering phases, indicating that not the BCC S.S. phase without chemical ordering, but the BCC phase with a B2-ordering structure was the main phase in melt-spun ribbons in $TiZrHfAlV_{0.2}$.

Fig. 12 shows a STEM BF image and electron dispersive spectroscopy (EDS) element mapping of the melt-spun ribbons of $TiZrHfAlV_{0.2}$. Table 2 shows the chemical composition analysis at positions B, A1, and A2 in Fig. 12. The matrix phase (B) contained all the constituent elements, indicating the formation of a multi-component BCC phase with a B2-ordering structure. Al and Zr were more enriched with precipitates embedded in the grain (A1) and at the grain boundaries (A2) compared with the matrix (B). A significant difference in the composition between locations A1 and A2 was not observed. In XRD patters (Fig. 9), the position of the minor (non-BCC) peaks do not correspond to the various Zr-Al-based intermetallic compounds. Further identification of the multi-component compounds (A1 and A2) based on the known intermetallic compounds was not achieved. The solidification microstructure analysis results in $TiZrHfAlV_{0.2}$ clarified the formation of the composite structure with a main phase of multicomponent BCC with a B2-ordering structure and minor Zr-Al-rich multicomponent precipitates in the rapidly-solidified melt-spun ribbons.

Table 3 shows the value of H_V and main constituent phases in the arc-melted ingots (a) for the TiZrHfAl MEA, $TiZrHfAlNb_{0.2}$ and $TiZrHfAlV_{0.2}$ HEAs, together with TiNbTaZrV and TiNbTaZrW RHEAs [56], TiZrNbTa [15,56] medium high-entropy alloys for metallic biomaterials (BioMEAs), TiZrNbTaMo [15,56] and $TiZrHfCo_{0.07}Cr_{0.07}Mo$ [20] BioHEAs as references, and melt-spun ribbons (b) for the TiZrHfAl MEA,

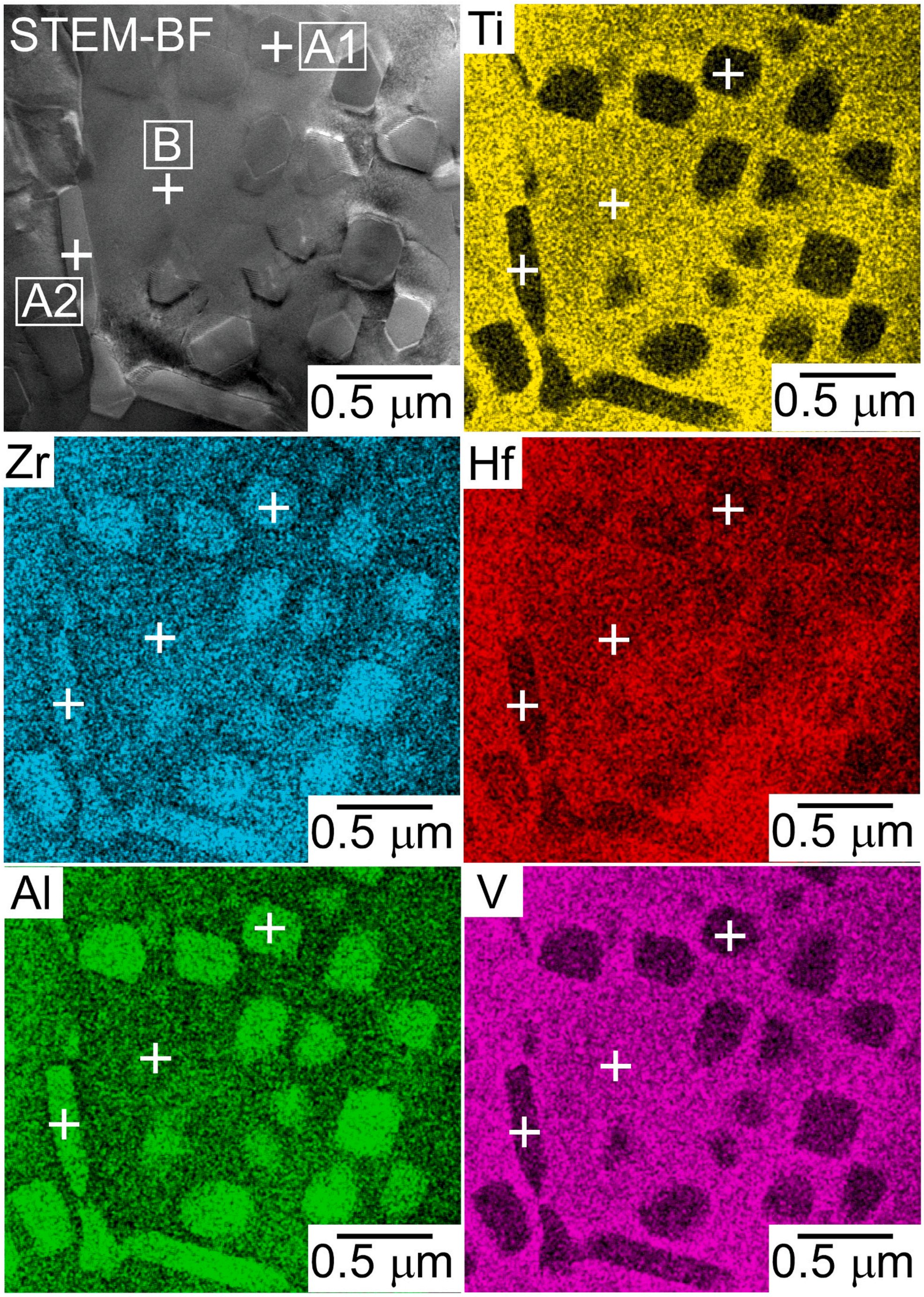

Fig. 12. Scanning transmission electron microscopy (STEM) bright field (BF)-image and STEM-electron dispersive spectroscopy (EDS) element mapping of the melt-spun ribbons in $TiZrHfAlV_{0.2}$.

Table 2
Chemical composition analysis results in melt-spun ribbons of $TiZrHfAlV_{0.2}$ by scanning transmission electron microscopy-electron dispersive spectroscopy (STEM-EDS).

Regions	Ti	Zr	Hf	Al	V
B	25.5	25.0	24.7	18.0	6.8
A1	12.4	36.3	20.0	28.8	2.4
A2	12.4	33.7	20.7	30.5	2.7

$TiZrHfAlNb_{0.2}$ and $TiZrHfAlV_{0.2}$ HEAs. The value of H_V in the arc-melted ingots was much higher than that in melt-spun ribbons for the TiZrHfAl MEA, $TiZrHfAlNb_{0.2}$, and $TiZrHfAlV_{0.2}$ HEAs. The values of H_V in the intermetallic compounds in the arc-melted ingots in TiZrHfAl MEA, $TiZrHfAlNb_{0.2}$, and $TiZrHfAlV_{0.2}$ HEAs shows the tendency to be higher than those in BCC phases in the other RHEAs and BioHEAs shown in Table 3a. The significantly high values of H_V in the arc-melted ingots for the TiZrHfAl MEA, $TiZrHfAlNb_{0.2}$ and $TiZrHfAlV_{0.2}$ HEAs can be explained by the formation of the intermetallic compounds as the main constituent phases. The values of H_V in arc-melted ingots of $TiZrNbTaX_1$ (X_1 = V, Mo, W) were reported to increase with increasing liquidus temperature T_L [56]. The T_L values in TiZrHfAl MEA, $TiZrHfAlNb_{0.2}$, and

Table 3
Micro-Vickers hardness (H_V) and main constituent phases of arc-melted ingots (a) and melt-spun ribbons (b) in TiZrHfAl MEA, $TiZrHfAlNb_{0.2}$ and $TiZrHfAlV_{0.2}$ HEAs, together with that in the arc-melted ingots of TiNbTaZrV and TiNbTaZrW RHEAs [56], TiZrNbTa [15,56] medium high-entropy alloys for metallic biomaterials (BioMEAs), TiZrNbTaMo [15,56] and $TiZrHfCo_{0.07}Cr_{0.07}Mo$ [20] BioHEAs as references.

(a) Arc-melted ingots		
Alloys	Main constituent phase	Hv
TiZrHfAl	Intermetallics	637
TiZrHfAlV0.2	Intermetallics	624
TiZrHfAlNb0.2	Intermetallics	551
TiNbTaZr	BCC	313
TiNbTaZrV	BCC	430
TiNbTaZrMo	BCC	477
TiNbTaZrW	BCC	556
TiZrHfCo0.07Cr0.07Mo	BCC	493
(b) Melt-spun ribbons		
Alloys		Hv
TiZrHfAl	BCC	315
TiZrHfAlV0.2	BCC	319
TiZrHfAlNb0.2	BCC	285

$TiZrHfAlV_{0.2}$ HEAs (Fig. 8) were much lower than those of $TiZrNbTaX_1$ (X_1 = V, Mo, W) [56]. The lower values of H_V of BCC phases in TiZrHfAl MEA, $TiZrHfAlNb_{0.2}$, and $TiZrHfAlV_{0.2}$ HEAs than those of BCC phase in $TiZrNbTaX_1$ (X_1 = V, Mo, W) may be related to the value of T_L. However, further investigation using additional experimental data is necessary for clarifying this tendency and will be performed in future studies.

In TiZrHfAl, $TiZrHfAlNb_{0.2}$, and $TiZrHfAlV_{0.2}$ alloys, S.S. formation was not detected in the arc-melted ingots by XRD patterns (Fig. 9), indicating that the rapid solidification was significantly effective to suppress the formation of intermetallics. The BCC phase with the B2-ordering structure was observed in rapidly-solidified melt-spun ribbon in $TiZrHfAlV_{0.2}$, but the chemical ordering structure was not predicted to form by the thermodynamic calculations (Figs. 4 and 5). The difficulty of predicting the formation of the B2 ordered structure in HEAs by CALPHAD has been noted in literature [65]. Various theoretical studies for the prediction of the B2-ordered phase in HEAs were challenged [66–69]; however, little is known about the B2-ordered structure formation in HEAs. The present study also demonstrated this difficulty. Further theoretical and experimental studies are warranted to examine the BCC/HCP solid solution formation and B2 ordering. The thermodynamic database used in the present study (SGTE2017) [52] was not sufficient to predict the thermal equilibrium phase because of the lack of the binary alloy system among Ti, Zr, Hf, Al, Nb and V, especially for binary Hf-Al and Hf-V pairs. Expansion of the thermodynamic database of Hf is necessary to elucidate the BCC/HCP phase selection and B2 ordering structure formation tendency in BCC phase in (Ti, Zr, Hf)-Al based alloys. This investigation will be performed in the future studies.

Focusing on the phase formation processes in three alloys (namely, TiZrHfAl, $TiZrHfAlNb_{0.2}$, and $TiZrHfAlV_{0.2}$), intermetallic compounds formation was observed in the arc-melted ingots regardless of the alloy system (Fig. 9). The elemental distribution due to the segregation and typical dendrite structure was not detected by EPMA-WDS analysis (Fig. 9, inset) in the arc-melted ingots. The multicomponent intermetallic phase was considered to form via solidification in these alloys, and the solidification microstructure analysis results were explained by this assumption without any discrepancy. The main constituent phases in rapidly solidified melt-spun ribbons in these alloys were not intermetallic compounds, which were observed in arc-melted ingots, but BCC phase with B2 ordering (Figs. 10 and 11). The high cooling rate during the single-roller melt-spinning process effectively suppressed the crystallization of the thermal melt to intermetallic compounds. The BCC phase formed from the thermal melt without significant elemental distribution. Fine precipitates were embedded in both intergranular regions and grain boundary regions (Figs. 11 and 12). The formation of the Zr- and Al- rich precipitates can be explained by the precipitation from BCC matrix during cooling after solidification in the single-roller melt-spinning process.

Recently, we firstly realized the fabrication of the alloy powders and the additive manufacturing (AM) via Selective Laser Melting (SLM) process of Ti-Nb-Ta-Zr-Mo BioHEAs [70], indicating that the rapid solidification via AM can be applicable in RHEAs and BioHEAs with 4th subgroup elements (Ti, Zr, Hf) as the main constituent elements. The *CR* during the solidification via SLM has been estimated as the order of 10^5 K/s – 10^7 K/s in literatures [71,72], implying that specimens with BCC structure may be obtained via SLM in TiZrHfAl MEA, $TiZrHfAlNb_{0.2}$ and $TiZrHfAlV_{0.2}$ HEAs. The control and customization of the fine microstructure in Ti and Ti-based alloys including BioHEAs was reported to be effective in the control of osteoblasts [70,73–75], and this implies the possibility of the enhancement of the biocompatibility in Ti-based BioHEAs by the formation of fine dispersions. The application of the SLM and the control of the dispersions in (Ti, Zr, Hf)-Al-based MEAs and HEAs will be reported in future works. Finally, it should be emphasized that the present study demonstrates the possibility of new alloy systems in RHEAs and/or BioHEAs with 4th subgroup elements (Ti, Zr, Hf) and Al as main constituent elements via rapid solidification technique.

5. Conclusions

The combination of 4th subgroup elements (Ti, Zr, Hf) and Al was investigated for the development of new MEA and HEA alloy systems. The results are summarized as follows.

(1) TiZrHfAl MEA, $TiZrHfAlNb_{0.2}$, and $TiZrHfAlV_{0.2}$ HEAs were designed by combining the 4th subgroup elements (Ti, Zr, Hf) with Al.
(2) The tendency to form a solid solution in TiZrHfAl MEA, and $TiZrHfAlNb_{0.2}$ and $TiZrHfAlV_{0.2}$ HEAs was predicted using empirical alloy parameters, predicted phase diagrams from Materials Project, and CALPHAD using FactSage and the SGTE2017 database.
(3) Rapid solidification was effective to suppress the formation of intermetallics, resulting in the BCC phase formation in the rapidly-solidified specimens of melt-spun ribbons in TiZrHfAl MEA, and $TiZrHfAlNb_{0.2}$ and $TiZrHfAlV_{0.2}$ HEAs.
(4) Electron microscopy observation clarified the formation of the composite structure with a main multicomponent BCC phase with B2-ordering structure and minor Zr-Al-rich multicomponent precipitates in the rapidly-solidified melt-spun ribbons of $TiZrHfAlV_{0.2}$ HEA.
(5) The micro-Vickers hardness, H_V, in arc-melted ingots was much larger than those in melt-spun ribbons in TiZrHfAl MEA, and $TiZrHfAlV_{0.2}$, and $TiZrHfAlNb_{0.2}$ HEAs, regardless the alloy system. This tendency can be explained by the differences in the constituent phases between arc-melted ingots and melt-spun ribbons in TiZrHfAl MEA, and $TiZrHfAlV_{0.2}$, and $TiZrHfAlNb_{0.2}$ HEAs. The values of H_V in BCC phases of the melt-spun ribbons in TiZrHfAl MEA, and $TiZrHfAlV_{0.2}$, and $TiZrHfAlNb_{0.2}$ HEAs were lower than those in BCC phases in arc-melted ingots of $TiZrNbTaX_1$ (X_1 = V, Mo, W) HEAs.

CRediT authorship contribution statement

Takeshi Nagase: Conceptualization, Investigation, Formal analysis, Writing – original draft. **Mitsuharu Todai:** Conceptualization, Writing – review & editing. **Pan Wang:** Writing – review & editing. **Shi-Hai Sun:** Writing – review & editing. **Takayoshi Nakano:** Supervision, Conceptualization, Writing – review & editing.

Declaration of competing interest

The authors declare that they have no known competing financial interests or personal relationships that could have appeared to influence the work reported in this paper.

Acknowledgements

Funding: This work was supported by JSPS KAKENHI (grant numbers 18H05254, 21H00146); the Council for Science, Technology and Innovation (CSTI); the Cross-Ministerial Strategic Innovation Promotion Program (SIP); the Innovative Design/Manufacturing Technologies program (Establishment and Validation of the Base for 3D Design and Additive Manufacturing Standing on the Concepts of "Anisotropy" and "Customization") of the New Energy and Industrial Technology Development Organization (NEDO); and the Light Metal Educational Foundation, Inc. Japan.

References

[1] B. Cantor, I.T.H. Chang, P. Knight, A.J.B. Vincent, Microstructural development in equiatomic multicomponent alloys, Mater. Sci. Eng. A 375–377 (2004) 213–218, https://doi.org/10.1016/j.msea.2003.10.257.
[2] J.W. Yeh, S.K. Chen, S.J. Lin, J.Y. Gan, T.S. Chin, T.T. Shun, C.H. Tsau, S.Y. Chang, Nanostructured high-entropy alloys with multiple principal elements: novel alloy design concepts and outcomes, Adv. Eng. Mater. 6 (2004) 299–303, https://doi.org/10.1002/adem.200300567.
[3] S. Ranganathan, Alloyed pleasures: multimetallic cocktails, Curr. Sci. 85 (2003) 1404–1406. https://www.currentscience.ac.in/Downloads/article_id_085_10_1404_1406_0.pdf.
[4] Y. Zhang, Y.J. Zhou, J.P. Lin, G.L. Chen, P.K. Liew, Solid-solution phase formation rules for multi-component alloys, Adv. Eng. Mater. 10 (2008) 534–538, https://doi.org/10.1002/adem.200700240.
[5] D.B. Miracle, O.N. Senkov, A critical review of high entropy alloys and related concepts, Acta Mater. 122 (2017) 448–511, https://doi.org/10.1016/j.actamat.2016.08.081.
[6] B.S. Murty, J.-W. Yeh, S. Ranganathan, High-Entropy Alloys, first ed., Elsevier, 2014.
[7] M.C. Gao, J.-W. Yeh, P.K. Liaw, Y. Zhang, High-Entropy Alloys, Fundamentals and Applications, first ed., Springer, 2016.
[8] B. Gludovatz, A. Hohenwarter, D. Catoor, E.H. Chang, E.P. George, R.O. Ritchie, A fracture-resistant high-entropy alloy for cryogenic applications, Science 345 (2014) 1153–1158, https://doi.org/10.1126/science.1254581.
[9] Z. Li, K.G. Pradeep, Y. Deng, D. Raabe, C.C. Tasan, Metastable high-entropy dual-phase alloys overcome the strength-ductility trade-off, Nature 534 (2016) 227–231, https://doi.org/10.1038/nature17981.
[10] O.N. Senkov, G.B. Wilks, D.B. Miracle, C.P. Chuang, P.K. Liaw, Refractory high-entropy alloys, Intermetallics 18 (2010) 1758–1765, https://doi.org/10.1016/j.intermet.2010.05.014.
[11] O.N. Senkov, G.B. Wilks, J.M. Scott, D.B. Miracle, Mechanical properties of $Nb_{25}Mo_{25}Ta_{25}W_{25}$ and $V_{20}Nb_{20}Mo_{20}Ta_{20}W_{20}$ refractory high entropy alloys, Intermetallics 19 (2011) 698–706, https://doi.org/10.1016/j.intermet.2011.01.004.
[12] O.N. Senkov, J.M. Scotta, S.V. Senkova, D.B. Miracle, C.F. Woodward, Microstructure and room temperature properties of a high-entropy TaNbHfZrTi alloy, J. Alloys Compd. 509 (2011) 6043–6048, https://doi.org/10.1016/j.jallcom.2011.02.171.
[13] O.N. Senkov, J.M. Scott, S.V. Senkova, F. Meisenkothen, D.B. Miracle, C. F. Woodward, Microstructure and elevated temperature properties of a refractory TaNbHfZrTi alloy, J. Mater. Sci. 47 (2012) 4062–4074, https://doi.org/10.1007/s10853-012-6260-2.
[14] O.N. Senkov, D.B. Miracle, K.J. Chaput, J.-P. Couzinie, Development and exploration of refractory high entropy alloys-A review, *J. Mater. Res.* 33 (2018) 3092–3128, https://doi.org/10.1557/jmr.2018.153.
[15] M. Todai, T. Nagase, T. Hori, A. Matsugaki, A. Sekita, T. Nakano, Novel TiNbTaZrMo high-entropy alloys for metallic biomaterials, Scripta Mater. 129 (2017) 65–68, https://doi.org/10.1016/j.scriptamat.2016.10.028.
[16] S.P. Wang, J. Xu, TiZrNbTaMo high-entropy alloy designed for orthopedic implants: as-cast microstructure and mechanical properties, Mater. Sci. Eng. C 73 (2017) 80–89, https://doi.org/10.1016/j.msec.2016.12.057.
[17] T. Nagase, M. Todai, T. Hori, T. Nakano, Microstructure of equiatomic and non-equiatomic Ti-Nb-Ta-Zr-Mo high-entropy alloys for metallic biomaterials, J. Alloys Compd. 753 (2018) 412–421, https://doi.org/10.1016/j.jallcom.2018.04.082.
[18] Y. Yuan, Y. Wu, Z. Yang, X. Liang, Z. Lei, H. Huang, H. Wang, X. Liu, K. An, W. Wu, Z. Lu, Formation, structure and properties of biocompatible TiZrHfNbTa high-entropy alloys, Mater. Res. Lett. 7 (2019) 225–231, https://doi.org/10.1080/21663831.2019.1584592.
[19] T. Hori, T. Nagase, M. Todai, A. Matsugaki, T. Nakano, Development of non-equiatomic Ti-Nb-Ta-Zr-Mo high-entropy alloys for metallic biomaterials, Scripta Mater. 172 (2019) 83–87, https://doi.org/10.1016/j.scriptamat.2019.07.011.
[20] T. Nagase, Y. Iijima, A. Matsugaki, K. Ameyama, T. Nakano, Design and fabrication of Ti-Zr-Hf-Cr-Mo and Ti-Zr-Hf-Co-Cr-Mo high-entropy alloys as metallic biomaterials, Mater. Sci. Eng. C 107 (2020), 110322, https://doi.org/10.1016/j.msec.2019.110322.
[21] T. Ishimoto, R. Ozasa, K. Nakano, M. Weinmann, C. Schnitter, M. Stenzel, A. Matsugaki, T. Nagase, T. Matsuzaka, M. Todai, H.S. Kim, T. Nakano, Development of TiNbTaZrMo bio–high entropy alloy (BioHEA) super–solid solution by selective laser melting, and its improved mechanical property and biocompatibility, Scripta Mater. 194 (2021), 113658, https://doi.org/10.1016/j.scriptamat.2020.113658.
[22] K.M. Youssef, A.J. Zaddach, C. Niu, D.L. Irving, C.C. Koch, A novel low-density, high-hardness, high-entropy alloy with close-packed single-phase nanocrystalline structures, Mater. Res. Lett. 3 (2015) 95–99, https://doi.org/10.1080/21663831.2014.985855.
[23] R. Feng, M.C. Gao, C. Lee, M. Mathes, T. Zuo, S. Chen, J.A. Hawk, Y. Zhang, P. K. Liaw, Design of light-weight high-entropy alloys, Entropy 18 (2016) 333, https://doi.org/10.3390/e18090333.
[24] Y. Qiu, Y.J. Hu, A. Taylor, M.J. Styles, R.K.W. Marceau, A.V. Ceguerra, M. A. Gibson, Z.K. Liu, H.L. Fraser, N. Birbilis, A lightweight single-phase AlTiVCr compositionally complex alloy, Acta Mater. 123 (2017) 115–124, https://doi.org/10.1016/j.actamat.2016.10.037.
[25] R. Feng, M.C. Gao, C. Zhang, W. Guo, J.D. Poplawsky, F. Zhang, J.A. Hawk, J. C. Neuefeind, Y. Ren, P.K. Liaw, Phase stability and transformation in a light-weight high-entropy alloy, Acta Mater. 146 (2018) 280–293, https://doi.org/10.1016/j.actamat.2017.12.061.
[26] T. Nagase, A. Terayama, T. Nagaoka, N. Fuyama, T. Sakamoto, Alloy design and fabrication of ingots of Al-Mg-Li-Ca light-weight medium entropy alloys, Mater. Trans. 61 (2020) 1369–1380, https://doi.org/10.2320/matertrans.F-M2020825.
[27] K.J. Laws, C. Crosby, A. Sridhar, P. Conway, L.S. Koloadin, M. Zhao, S. Aron-Dine, L.C. Bassman, High entropy brasses and bronzes - microstructure, phase evolution and properties, J. Alloys Compd. 650 (2015) 949–961, https://doi.org/10.1016/j.jallcom.2015.07.285.
[28] T. Nagase, A. Shibata, M. Matsumuro, M. Takemura, S. Semboshi, Alloy design and fabrication of ingots in Cu-Zn-Mn-Ni-Sn high-entropy and Cu-Zn-Mn-Ni medium-entropy brasses, Mater. Des. 181 (2019), 107900, https://doi.org/10.1016/j.matdes.2019.107900.
[29] L. Rogal, P. Bobrowski, F. Körmann, S. Divinski, F. Stein, B. Grabowski, Computationally-driven engineering of sublattice ordering in a hexagonal AlHfScTiZr high entropy alloy, Sci. Rep. 7 (2017) 2209, https://doi.org/10.1038/s41598-017-02385-w.
[30] G.-Y. Gan, L. Ma, D.-M. Luo, S. Jiang, B.-Y. Tang, Influence of Al substitution for Sc on thermodynamic properties of HCP high entropy alloy $Hf_{0.25}Ti_{0.25}Zr_{0.25}Sc_{0.25-x}Al_x$ from first-principles investigation, Mater. Des. 593 (2020), 412272, https://doi.org/10.1016/j.physb.2020.412272.
[31] S.G. Steineman, in: G.D. Winter, J.L. Leray, K. de Groot (Eds.), Corrosion of Surgical Implants-In Vivo and Vitro Tests, Evaluation of Biomaterials, John Willey & Sons Ltd., 1980.
[32] M.F. Semlitsch, H.W. Robert, M.S. RolfSchon, Joint replacement components made of hot-forged and surface-treated Ti-6Al-7Nb alloy, Biomaterials 13 (1992) 781–788, https://doi.org/10.1016/0142-9612(92)90018-J.
[33] Y. Okazaki, Development of Ti alloy for medical implants, J. Jpn. Inst. Light Metals 49 (1999) 613–620, https://doi.org/10.2464/jilm.49.613.
[34] K. Maehara, K. Doi, T. Matsushita, Y. Sasaki, Application of vanadium-free titanium alloys to artificial hip joints, Mater. Trans. 43 (2002) 2936–2942, https://doi.org/10.2320/matertrans.43.2936.
[35] X. Yang, Y. Zhang, Prediction of high-entropy stabilized solid-solution in multi-component alloys, Mater. Chem. Phys. 132 (2012) 233–238, https://doi.org/10.1016/j.matchemphys.2011.11.021.
[36] Y. Zhang, Z.P. Lu, S.G. Ma, P.K. Liaw, Z. Tang, Y.Q. Cheng, M.C. Gao, Guidelines in predicting phase formation of high-entropy alloys, MRS Commun 4 (2014) 57–62, https://doi.org/10.1557/mrc.2014.11.
[37] A. Takeuchi, A. Inoue, Classification of bulk metallic glasses by atomic size difference, heat of mixing and period of constituent elements and its application to characterization of the main alloying element, Mater. Trans. 46 (2005) 2817–2829, https://doi.org/10.2320/matertrans.46.2817.
[38] U.R. Kattner, J.-C. Lin, Y.A. Chang, Thermodynamic assessment and calculation of the Ti-Al system, Metall. Trans. A 23 (1992) 2081–2090, https://doi.org/10.1007/BF02646001.
[39] I. Ohnuma, Y. Fujita, H. Mitsui, K. Ishikawa, R. Kainuma, K. Ishida, Phase equilibria in the Ti-Al binary system, Acta Mater. 48 (2000) 3113–3123, https://doi.org/10.1016/S1359-6454(00)00118-X.
[40] M. Alatalo, M. Weinert, R.E. Watson, Stability of Zr-Al alloys, Phys. Rev. B 57 (1998) R2009–R2012, https://doi.org/10.1103/PhysRevB.57.R2009.
[41] T. Wang, Z. Jin, J.-C. Zhao, Thermodynamic assessment of the Al-Zr binary system, J. Phase Equil. 22 (2001) 544–551, https://doi.org/10.1007/s11669-001-0072-4.
[42] T. Wang, Z. Jin, J.-C. Zhao, Thermodynamic assessment of the Al-Hf binary system, J. Phase Equil. 23 (2002) 416–423, https://doi.org/10.1361/105497102770331361.
[43] L. L. Rokhlin, N. R. Bochvar, T. V. Dobatkina, V. G. Leontev: Al-rich portion of the Al-Hf phase diagram, Russ. Metall., 2009 (2009) 258-262., https://doi.org/10.1134/S0036029509030124.
[44] H. Okamoto, Al-V (Aluminum-Vanadium), J. Phase Equil. 33 (2012) 491, https://doi.org/10.1007/s11669-012-0090-4.
[45] C. Colinet, A. Pasturel, D. Nguyen Manh, D.G. Pettifor, P. Miodownik, Phase-stability study of the Al-Nb system, Phys. Rev. B 56 (1997) 552–565, https://doi.org/10.1103/PhysRevB.56.552.

[46] A. Jain, S.P. Ong, G. Hautier, W. Chen, W.D. Richards, S. Dacek, S. Cholia, D. Gunter, D. Skinner, G. Ceder, K.A. Persson, Commentary: the Materials Project: a materials genome approach to accelerating materials innovation, Apl. Mater. 1 (2013) 1, https://doi.org/10.1063/1.4812323, 011002.
[47] T. Nagase, M. Suzuki, T. Tanaka, Formation of amorphous phase with crystalline globules in Fe-Cu-Nb-B immiscible alloys, J. Alloys Compd. 619 (2015) 267–274, https://doi.org/10.1016/j.jallcom.2014.08.229.
[48] T. Nagase, P.D. Rack, J.H. Noh, T. Egami, In-situ TEM observation of structural changes in nano-crystalline CoCrCuFeNi multicomponent high-entropy alloy (HEA) under fast electron irradiation by high voltage electron microscopy (HVEM), Intermetallics 59 (2015) 32–42, https://doi.org/10.1016/j.intermet.2014.12.007.
[49] T. Nagase, M. Todai, T. Nakano, Development of Co-Cr-Mo-Fe-Mn-W and Co-Cr-Mo-Fe-Mn-W-Ag high-entropy alloys based on Co-Cr-Mo alloys, Mater. Trans. 61 (2020) 567–576, https://doi.org/10.2320/matertrans.MT-MK2019002.
[50] T. Nagase, M. Todai, T. Nakano, Development of Ti-Zr-Hf-Y-La high-entropy alloys with dual hexagonal-close-packed structure, Scripta Mater. 186 (2020) 242–246, https://doi.org/10.1016/j.scriptamat.2020.05.033.
[51] T. Nagase, M. Todai, T. Nakano, Liquid phase separation in Ag-Co-Cr-Fe-Mn-Ni, Co-Cr-Cu-Fe-Mn-Ni and Co-Cr-Cu-Fe-Mn-Ni-B high entropy alloys for biomedical application, Crystals 10 (2020) 527, https://doi.org/10.3390/cryst10060527.
[52] http://www.factsage.com/ assessed, August 25th, 2021.
[53] SGTE. http://www.crct.polymtl.ca/fact/documentation/SGTE2017/SGTE2017_Figs.htm (assessed, 2017. (Accessed 20 January 2020).
[54] E.W. Collings, Materials Properties Handbook Titanium Alloys, ASM International, 1994, p. 10.
[55] K. Ishida, Schaeffler-type phase diagram of Ti-based alloys, Metall. Mater. Trans. 48 (2017) 4990–4998, https://doi.org/10.1007/s11661-017-4218-3.
[56] T. Nagase, K. Mizuuchi, T. Nakano, Solidification microstructures of the ingots obtained by arc melting and cold crucible levitation melting in TiNbTaZr medium-entropy alloy and TiNbTaZrX (X = V, Mo, W) high-entropy alloys, Entropy 21 (2019) 483, https://doi.org/10.3390/e21050483.
[57] T. Nagase, M. Takemura, M. Matsumuro, T. Maruyama, Solidification microstructure of $AlCoCrFeNi_{2.1}$ eutectic high entropy alloy ingots, Mater. Trans. 59 (2018) 255–264, https://doi.org/10.2320/matertrans.F-M2017851.
[58] R.W. Cahn, Physical Metallurgy, third ed., Elsevier Science Publishers, 1996, ISBN 9780444898753.
[59] H. Miyake, A. Furusawa, T. Ariyasu, A. Okada, Optical measurement of cooling rate during splat cooling process, J. Jpn. Foundrymen's Soc. 66 (1994) 734–738, https://doi.org/10.11279/imono.66.10_734.
[60] C.G. Wilson, D. Sams, The crystal structure of Zr_2Al, Acta Crystallogr. 14 (1961) 71–72, https://doi.org/10.1107/S0365110X6100022X.
[61] M. Pang, Y. Zhan, W. Yang, C. Li, Y. Du, The phase relationships in the Al-Zr-Ho ternary system at 773 K, J. Alloys Compd. 508 (2010) 79–84, https://doi.org/10.1016/j.jallcom.2010.08.058.
[62] J. Ning, X. Zhang, J. Qin, S. Zhang, M. Ma, R. Li, Distinct electron density topologies and elastic properties of two similar omega phases: ω-Zr and Zr_2Al, J. Alloys Compd. 660 (2016) 316–323, https://doi.org/10.1016/j.jallcom.2015.11.114.
[63] Materials Projects, Zr_2Al, ID: mp-2557, https://doi.org/10.17188/1200766.
[64] K. Momma, F. Izumi, VESTA 3 for three-dimensional visualization of crystal, volumetric and morphology data, J. Appl. Crystallogr. 44 (2011) 1272–1276, https://doi.org/10.1107/S0021889811038970.
[65] D.B. Miracle, High entropy alloys as a bold step forward in alloy development, Nat. Commun. 10 (2019) 1805, https://doi.org/10.1038/s41467-019-09700-1.
[66] C. Li, M. Zhao, J.C. Li, Q. Jiang, B2 structure of high-entropy alloys with addition of Al, J. Appl. Phys. 104 (2008), 113504, https://doi.org/10.1063/1.3032900.
[67] W.P. Huhn, M. Widom, Prediction of A2 to B2 phase transition in the high-entropy alloy Mo-Nb-Ta-W, JOM 65 (2013) 1772–1779, https://doi.org/10.1007/s11837-013-0772-3.
[68] Z. Leong, J.S. Wrobel, S.L. Dudarev, R. Goodall, I. Todd, D. Nguyen-Manh, The effect of electronic structure on the phases present in high entropy alloys, Sci. Rep. 7 (2017) 39803, https://doi.org/10.1038/srep39803.
[69] L.J. Santodonato, P.K. Liaw, R.R. Unocic, H. Bei, J.R. Morris, Predictive multiphase evolution in Al-containing high-entropy alloys, Nat. Commun. 9 (2018) 4520, https://doi.org/10.1038/s41467-018-06757-2.
[70] T. Ishimoto, R. Ozasa, K. Nakano, M. Weinmann, C. Schnitter, M. Stenzel, A. Matsugaki, T. Nagase, T. Matsuzaka, M. Todai, H.S. Kim, T. Nakano, Development of TiNbTaZrMo bio–high entropy alloy (BioHEA) super–solid solution by selective laser melting, and its improved mechanical property and biocompatibility, Scripta Mater. 194 (2021), 113658, https://doi.org/10.1016/j.scriptamat.2020.113658.
[71] Q. Jia, P. Rometsch, P. Kürnsteiner, Q. Chao, A. Huang, M. Weyland, L. Bourgeois, X. Wu, Selective laser melting of a high strength Al-Mn-Sc alloy: alloy design and strengthening mechanisms, Acta Mater. 171 (2019) 108–118, https://doi.org/10.1016/j.actamat.2019.04.014.
[72] D. Gu, Q. Shi, K. Lin, L. Xi, Microstructure and performance evolution and underlying thermal mechanisms of Ni-based parts fabricated by selective laser melting, Addit. Manuf. 22 (2018) 265–278, https://doi.org/10.1016/j.addma.2018.05.019.
[73] A. Matsugaki, G. Aramoto, T. Nakano, The alignment of MC3T3-E1 osteoblasts on steps of slip traces introduced by dislocation motion, Biomaterials 33 (2012) 7327–7335, https://doi.org/10.1016/j.biomaterials.2012.06.022.
[74] A. Matsugaki, G. Aramoto, T. Ninomiya, H. Sawada, S. Hata, T. Nakano, Abnormal arrangement of a collagen/apatite extracellular matrix orthogonal to osteoblast alignment is constructed by a nanoscale periodic surface structure, Biomaterials 37 (2015) 134–143, https://doi.org/10.1016/j.biomaterials.2014.10.025.
[75] Y. Nakanishi, A. Matsugaki, K. Kawahara, T. Ninomiya, H. Sawada, T. Nakano, Unique arrangement of bone matrix orthogonal to osteoblast alignment controlled by Tspan11-mediated focal adhesion assembly, Biomaterials 209 (2019) 103–110, https://doi.org/10.1016/j.biomaterials.2019.04.016.